PAPER • OPEN ACCESS

The role of RF-induced E×B flows in the mitigation of scrape-off-layer convective transport during ion cyclotron resonance heating

View the article online for updates and enhancements.

The role of RF-induced E×B flows in the mitigation of scrape-off-layer convective transport during ion cyclotron resonance heating

R. Diab[1,*] ID, G. Decristoforo[2] ID, S. Ahmed[2] ID, S.G. Baek[1], Y. Lin[1], E. Marmar[1], J.L. Terry[1] ID and S.J. Wukitch[1]

[1] MIT Plasma Science and Fusion Center, Cambridge, MA 02139, United States of America
[2] Department of Physics and Technology, UiT The Arctic University of Norway, NO-9037 Tromsø, Norway

E-mail: diab@mit.edu

CrossMark

Abstract
While multiple experiments have reported a decrease in intermittent fluctuations in the far Scrape-Off-Layer (SOL) during ion cyclotron resonance heating (Antar *et al* 2010 *Phys. Rev. Lett.* **105** 165001, Li *et al* 2022 *Nucl. Eng. Technol.* **54** 207–19, Antar *et al* 2012 *Nucl. Fusion* **52** 103005), the physical mechanism behind this observation has not been fully established yet. In this work, we demonstrate, for the first time, a direct correlation between the amplitude of RF-induced E×B flows and turbulence suppression in the far SOL. Using the Gas Puff Imaging (GPI) diagnostic on Alcator C-Mod, we show again that Ion Cyclotron Range of Frequencies can significantly alter the flow in the SOL and introduce a shear layer in regions magnetically connected close to the antenna (Cziegler *et al* 2012 *Plasma Phys. Control. Fusion* **54** 105019). With the 4-strap field-aligned antenna operated in dipole phasing, the ratio of the power coupled by the central two straps to the power coupled by the outer two straps was varied. The resulting RF-induced radial electric field magnitude thus varied, and we show that the impact on the far SOL turbulence correlates with the modified E×B velocity. We then apply a newly-developed blob tracking algorithm (Han *et al* 2022 *Sci. Rep.* **12** 18142) to higher-resolution GPI videos in order to directly observe the process of blob shearing by RF-induced E×B flows. We show that the radially sheared poloidal flows act as a transport barrier by stretching, stopping, and destroying filaments, which is consistent with the observed difference in turbulence statistics.

Keywords: ICRF, turbulence, transport, RF sheath, gas puff imaging, blob tracking, Alcator C-Mod

(Some figures may appear in colour only in the online journal)

---

* Author to whom any correspondence should be addressed.

1. Introduction

Ion Cyclotron Range of Frequencies (ICRF) heating is one of the auxiliary heating methods capable of achieving thermonuclear fusion-relevant temperatures in magnetically confined plasmas and is envisioned as an essential component of next-generation fusion devices like SPARC and ITER [1, 2]. However, due to the evanescence of the ICRF fast wave in vacuum, efficient coupling requires positioning ICRF antennas close to the plasma edge, where enhanced RF-plasma interaction can occur. The study of this interaction is generally complicated by its inherently intertwined nature, since ICRF heating can modify the edge plasma properties and, in turn, the edge plasma properties affect the coupling of ICRF waves to the core plasma. In addition to increased impurity generation and local plasma heating in the Scrape-Off Layer (SOL), complex changes to the density profile have been observed [3], with different experiments reporting a local increase or decrease in plasma density depending on the radial and poloidal mapping to the active ICRF antenna. A density depletion is typically observed near the antenna limiter edge, sometimes accompanied by a density increase at smaller or larger major radii [4–11]. Moreover, ICRF-induced poloidal asymmetries in the density profile have been observed, for example, in Tore Supra [9], JET [10], Phaedrus-T [5], LAPD [12], and Alcator C-Mod [11, 13]. This complex density distribution could be seen to either improve or degrade lower hybrid (LH) wave coupling depending on the magnetic connection to the active ICRF antenna [8, 11, 14].

Another observation common to most ICRF experiments is the formation of E×B plasma flows across field lines connecting to the active antenna. Such flows were directly measured using Gas Puff Imaging (GPI) in multiple Alcator C-Mod experiments [15–17] among others. Their origin can be understood as follows: due to the faster motion of electrons (with respect to ions) along field lines, parasitically-excited parallel RF electric fields on the antenna structure can enhance the local DC plasma potential via the RF rectification mechanism [18]. This is essentially a consequence of the non-linearity of the current–voltage (*I*–*V*) relationship at the sheath: an oscillating RF voltage will yield a net DC electron flux towards the metallic wall and the DC plasma potential will increase to satisfy ambipolarity. It is the differential biasing of neighboring flux tubes by RF rectification that eventually leads to radial and poloidal electric fields and E×B convection. While ICRF-related modifications of the edge density distribution might be influenced by multiple processes (an increase in the particle flux from the wall, enhanced ionization rate due to local plasma heating, ponderomotive forces, etc), these RF-induced E×B flows have long been thought to play an important role [8, 11–13, 19]. This motivated the need for a better understanding of how these flows modify radial transport in the SOL, which is the subject of this paper.

Cross-field transport in the SOL was shown to be dominated by the convective radial motion of field-aligned filamentary structures (commonly called 'blobs') that are intermittently injected into the SOL [20–22]. Multiple experiments have shown that these intermittent fluctuations can be strongly

mitigated by ICRF heating. In CHS, a net decrease in the fluctuation level was observed in the SOL when the ICRF power exceeded 300 kW [23]. Later, on ASDEX-U, ICRF heating was shown to suppress SOL convective transport in between ELMs and reduce ELM-induced transport [24]. Similar observations were made in Tore-Supra [25] and EAST [26], where ICRF heating was shown to mitigate SOL intermittent transport on field lines magnetically connected to the vicinity of ICRF antennas. This was also shown in [27], where it was further suggested that ICRF can interact nonlinearly with turbulence via parametric decay instabilities. While a reduction in intermittent fluctuations in the far SOL is ubiquitously observed in ICRF experiments, the physical mechanism behind it has not been fully established previously.

In this paper, we provide a direct observation of blob shearing by RF-induced E×B flows and show that it can explain the observed reduction in convective transport. In section 2, the experimental setup and diagnostics are presented. In section 3, we demonstrate a method for controlling ICRF-induced E×B flows and establish, for the first time, a correlation between the amplitude of these flows and the mitigation of intermittent fluctuations in the far SOL. In section 4, we use high-resolution GPI videos and a novel blob-tracking algorithm [28] to directly observe the process of blob shearing by ICRF-induced flows. Conclusions will be given in section 5.

2. Experimental setup and diagnostics

The experiments were performed on Alcator C-Mod, a compact (major radius $R_0 = 0.67$ m, minor radius $a = 0.22$ m) high-field (up to 8.1 T on-axis) diverted tokamak in which the plasma-facing components consisted of high-Z molybdenum tiles [29]. C-Mod had three ICRF antennas located at D, E, and J ports (shown in figure 3). The D and E antennas were classic two-strap toroidally-aligned (TA) antennas, i.e. whose straps were perpendicular to the toroidal magnetic field. Before 2012, the J antenna was a four-strap TA antenna. In early 2012, it was replaced with a novel field-aligned (FA) antenna, whose straps were perpendicular to the total background magnetic field (for $q_{95} \sim 3.8$) [16]. Section 3 will study discharges heated with the FA J antenna while section 4 will focus on a discharge heated with the D antenna.

To study edge turbulence, we use two in-vessel imaging diagnostics monitoring the He I (587.6 nm) line emission from a local helium gas cloud puffed by a nozzle just below the outboard midplane: these are the so-called GPI diagnostics. In section 3, we study data from the GPI-APD diagnostic [30], which consists of an array of 9×10 optical fibers coupled to fast avalanche photodiode detectors with a 2 MHz sampling rate. In section 4, we study data from the GPI-Phantom diagnostic [31], a fast-camera-based system with a higher spatial resolution ($\sim$2 mm vs $\sim$4 mm for GPI-APD) and larger field-of-view ($\sim$62 mm × $\sim$62 mm vs. $\sim$40 mm × $\sim$44 mm for GPI-APD) but a smaller time resolution (390.8 kHz sampling rate). Although inferior to the APD detectors for studying turbulence statistics, the GPI Phantom system is a useful tool for observing and tracking

SOL filaments. The estimated spatial resolution of each line of sight for each of C-Mod's GPI systems is determined by the pixel (or fiber) size, the imaging systems' magnifications and image quality, and the toroidal distribution of emission in front of the nozzle where the sightlines pass through the puffed gas cloud. Note that the dimensions of the fields-of-view are not the spatial resolutions times the number of pixels since each pixel's field-of-view overlaps to some extent with its neighbors'.

Both GPI diagnostics on Alcator C-Mod utilize the same nozzle at the outboard midplane that has four vertically stacked gas channels, all fed by a single 1 mm diameter capillary. Gas is injected perpendicular to the toroidal field and emissions are detected using in-vessel optics that view the gas puff tangentially and couple the detected light to fibers that bring the images to the multi-element detectors. The sight lines for the GPI-Phantom system are typically within 3 degrees of the magnetic field lines local to the gas cloud, while those of the GPI-APD system are horizontal and view the cloud at 7–10 degrees with respect to the local field lines. For these experiments, neutral helium gas was puffed. No measurement of the toroidal extent of gas from this nozzle has been made. Our estimates of the toroidal extent are based on post-experimental lab measurements made using a single 1 mm diameter capillary at a typical backing pressure. We estimate the extent to be 2.5 cm at the key region examined in this study, i.e. $R \sim 90.5$ cm (see, for example, figure 5). This toroidal extent would lead to a smearing of 1 mm for the GPI-Phantom and 3–4 mm for the GPI APD. A DEGAS 2 Monte Carlo modeling has been conducted to investigate this chord-integration effect [32]. None of the conclusions of this paper depend on the exact accuracy of these estimates.

Note that the GPI diagnostics measure the visible light emitted by line radiation in a neutral gas (which is itself a function of plasma density and temperature) but do not provide a direct measurement of density or temperature fluctuations. However, line emission fluctuations are typically assumed to be a good proxy for electron density fluctuations in the SOL, where density fluctuations from radially- and poloidally-propagating filaments are expected to be large and have very similar properties to the line radiation fluctuations measured by GPI [31]. On Alcator C-Mod, line emission fluctuations measured by GPI and ion saturation current fluctuations measured by Langmuir probes typically showed very good agreement, with cross-correlation values exceeding 75% in some cases [22]. Figure 1 shows a poloidal cross-section of Alcator C-Mod with the GPI field of view.

3. Impact of ICRF and antenna power ratio on turbulence statistics

In this section, we compare five discharges (1160926034, 35, 37, 38, and 39) in the Lower Single Null (LSN) configuration with similar plasma shape, toroidal magnetic field ($B_T = 5.2$ T on-axis), plasma current ($I_p = 0.9$ MA), and line-averaged density ($\bar{n}_e \approx 1.15 \times 10^{20}$ m^{-3}).
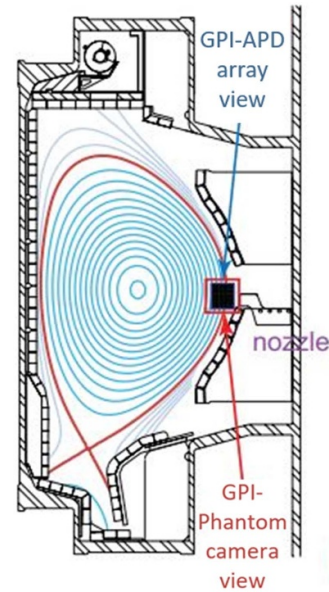

Figure 1. Poloidal cross-section of the Alcator C-Mod tokamak showing the location of the nozzle and the fields of view of the GPI diagnostics (not to scale). A view of the outer wall with magnetic connections to the antennas is shown in figure 3.
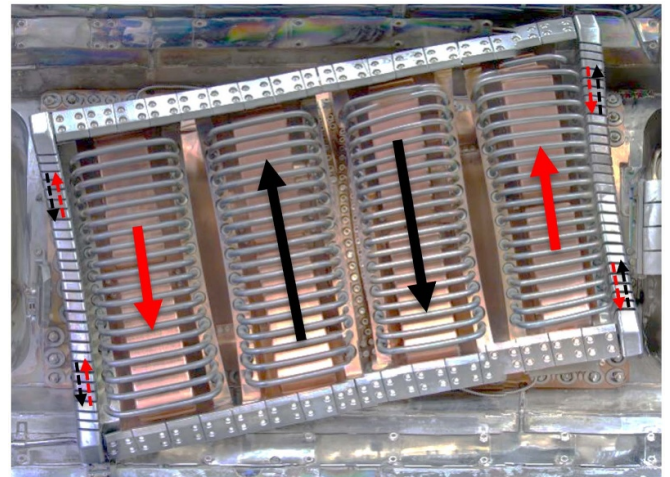

Figure 2. Photo of the Alcator C-Mod four-strap field-aligned J antenna illustrating the principle of power ratio modulation. With the antenna operated in dipole phasing ($0\pi 0\pi$), by putting more power in the central two straps than in the outer two straps, the image currents resulting from the two pairs of straps can be minimized and in principle canceled for a range of P_{cent}/P_{tot}.

During these experiments, the four-strap FA J antenna was operated in dipole phasing ($0\pi 0\pi$) with the central two straps as one pair and the outer two straps as another pair, and the ratio of the power coupled by the central and outer straps was varied. In the rest of the paper 'power ratio' will refer to the ratio of the power injected by the central two straps to the total injected ICRF power: P_{cent}/P_{tot}. The idea behind power ratio modulation is illustrated in figure 2 and is inspired by the ASDEX-U three-strap antenna experiments [33, 34]: the antenna is operated in dipole phasing with higher power
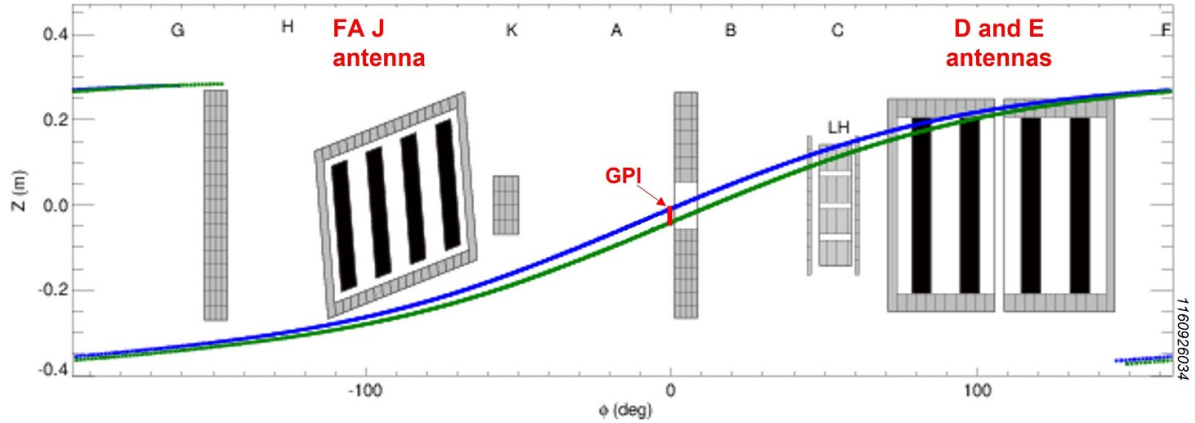
Figure 3. Unfolded view of the Alcator C-Mod outer wall showing magnetic field line connections from the GPI field of view to the antennas. The structures shown are (left to right): a poloidal limiter, the FA-J antenna, a partial limiter, the GPI nozzle mounted on a 'split' poloidal limiter, the lower hybrid wave launcher, the D-port TA antenna, and the E-port TA antenna. The blue and green field lines pass through the top and bottom of the GPI field of view respectively.

coupled through the center two straps than the outer two straps, thus minimizing the induced RF currents (so-called image currents) on the antenna limiters. These RF currents are closest to the plasma and, at the corners of the antenna box, they have a large parallel component, hence leading to large parallel RF electric fields $E_{||}$. These RF electric fields can enhance the DC plasma potential via the RF rectification mechanism. As explained earlier, it is the inhomogeneous distribution of RF-enhanced DC plasma potentials that is responsible for E×B plasma flows. Hence, by scanning P_{cent}/P_{tot}, the limiter induced currents and the RF-induced radial electric field amplitudes are varied, offering a path to control the magnitude of RF-induced E×B flows.

In these five discharges, the GPI field of view magnetically maps to a narrow region just below one of the corners of the field-aligned J antenna, as shown in figure 3. As shown previously on multiple devices (notably Alcator C-Mod [15–17, 35], Tore Supra [8, 9], WEST [36], or ASDEX-U [37]) the ICRF-enhanced potential and poloidal velocity structures can be quite extended beyond the leading edge of antenna limiters, both radially and poloidally, with a peak typically located close to the corners of the antenna [18]. Moreover, [25, 26] have shown that direct magnetic connection to the antenna is not necessary to see changes in turbulent fluctuations during ICRF heating, in the sense that magnetically connecting close enough to the antenna is sufficient. As we will later show, the GPI mapping to the antenna in the case presently studied is close enough to measure significant differences in the E×B poloidal velocity profiles, with velocities as high as $6\,\mathrm{km\,s^{-1}}$ in some cases, which is an order of magnitude higher than the velocities measured with no RF. Consequently, the change in SOL turbulence due to the radially sheared E×B flow will be unambiguously measured.

The first four aforementioned discharges (# 34, 35, 37, and 38) are all heated with a 1 MW pulse of ICRF (using the four-strap FA J antenna) from $t = 0.9\,\mathrm{s}$ to $t = 1.2\,\mathrm{s}$, but with different power ratios (respectively 0.70, 0.35, 0.2, and 0.8). Discharge # 39 has no RF pulse.

First, we aim to assess the impact of ICRF heating and antenna P_{cent}/P_{tot} on the SOL flow. To do so, we apply a simple cross-correlation velocimetry technique to each column of GPI-APD views so as to obtain a radial profile of the poloidal velocity. In each column, we pick two views separated by $\Delta Z \approx 0.75\,\mathrm{cm}$. For each pair of views, we calculate the cross-correlation of the detected signal over a moving time window of $\approx 100\,\mu\mathrm{s}$. This is shown in figure 4(*b*), where we plot examples of cross-correlation functions calculated within a $100\,\mu\mathrm{s}$ time interval at $R \approx 90.69\,\mathrm{cm}$ for the five different cases studied. The poloidal velocity in each $100\,\mu\mathrm{s}$ interval (which is approximately equal to the vertical velocity for these views located close to the midplane) is then estimated by dividing the distance between the two views by the time lag τ_{max} corresponding to the maximum cross-correlation value, i.e. $v_\theta \approx \Delta Z/\tau_{max}$. The mean poloidal velocity at each radial position is then calculated by taking the average of the estimated velocities for cases where the time-delayed cross-correlation value is larger than 0.7. Figure 4 shows the (R, Z) locations where the APD-based GPI sightlines pierce the poloidal plane at the center of the gas cloud. The views used for the velocity calculation are highlighted in red. Note that multiple views (represented in black) were dead during the experiment presently studied. With the views considered here, the maximum measurable poloidal velocity is $\approx 15\,\mathrm{km\,s^{-1}}$, which is at least a factor of 2 larger than the biggest poloidal velocities typically measured in such experiments [15–17]. Hence, in the present calculation, cases with a time lag of 0 are attributed to structures that are much larger than the distance between the two views.

The estimated poloidal velocity profiles are shown in figure 5. In the absence of ICRF, the poloidal velocity is slightly negative (downward) everywhere in the SOL. With ICRF, the poloidal velocity in the far-SOL switches sign, leading to a radially-sheared poloidal flow. As expected, for a constant ICRF power of 1 MW, the amplitude of the E×B velocity is reduced when increasing P_{cent}/P_{tot} from 0.2 to 0.8, which is consistent with the picture of image current mitigation. Also note the existence of another shear layer inside
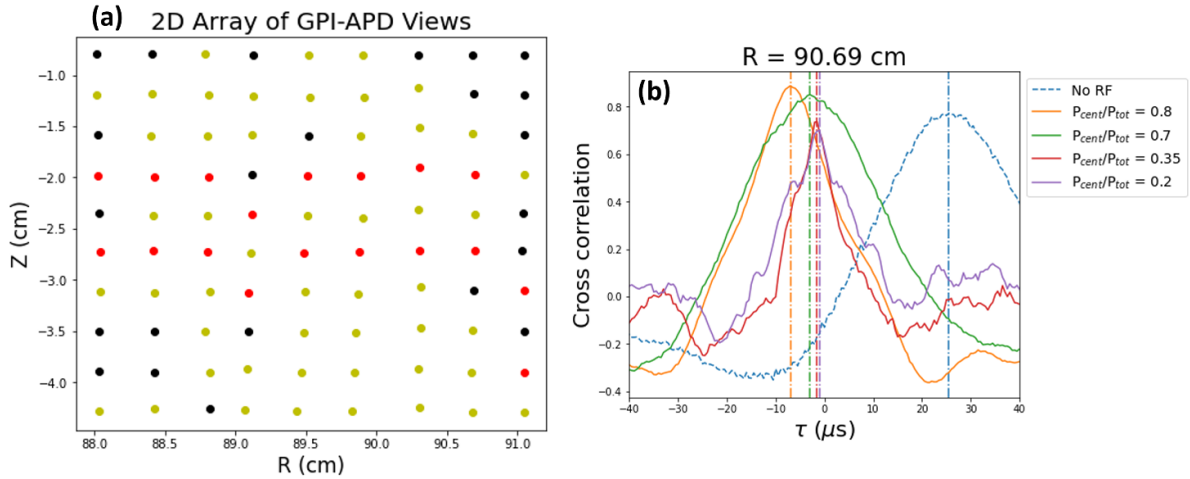
Figure 4. (*a*) Array of GPI-APD views. Red dots correspond to the centers of views used for the poloidal velocity estimation (2 for each radial position). Black dots correspond to broken fibers that no longer couple the light to the detectors. Other view centers are represented by yellow dots. (*b*) Examples of cross-correlation functions calculated within a 100 μs time interval at $R = 90.69$ cm for the five cases studied. The vertical dash-dotted lines indicate the time lags corresponding to the maximum cross-correlations.
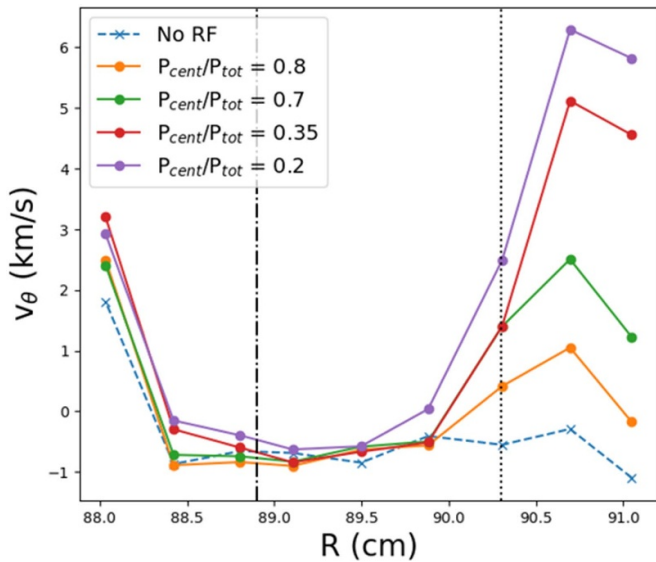

Figure 5. Poloidal velocity profiles estimated by cross-correlation analysis for the case without ICRF and the four cases with 1 MW of injected ICRF power and different power ratios. The vertical black dash-dotted line shows the position of the last closed flux surface estimated using EFIT. The vertical black dotted line shows the radial location of the lower corner of the J antenna limiter mapped to the poloidal plane containing the GPI field of view. The wall is located at $R = 108$ cm.

the separatrix that is present independently of the presence of ICRF. A more detailed analysis of the impact of power ratio on RF-enhanced potentials and antenna performance will be discussed in a separate study, while this paper will focus on the impact of P_{cent}/P_{tot} and RF-induced E×B flows on SOL turbulence. Specifically, in this section, we will perform a similar analysis to that shown in [23–26] to study the impact of ICRF on SOL turbulence, but we aim to show that this effect is directly correlated with antenna power ratio and, therefore, with the amplitude of RF-induced E×B flows.

To analyze the statistical properties of turbulence in the far SOL, we study the brightness data measured by an APD view at $(R, Z) = (91.045, -1.974)$ cm from $t = 0.91$ s to $t = 1.19$ s (280 ms time window during the 1 MW ICRF pulse) for the five selected discharges. To illustrate the impact of antenna power ratio on SOL turbulence, we show in figure 6 the measured data time series over a 10 ms time window for the different cases studied. The plotted quantity is $(I - \langle I \rangle)/\langle I \rangle$ where I is the detected brightness signal and $\langle I \rangle$ its mean value. Subtracting $\langle I \rangle$ ensures that the resulting signal has a vanishing mean, while normalizing by $\langle I \rangle$ eliminates amplitude variations due to small differences in puffing parameters and edge plasma heating by ICRF. We can see that decreasing P_{cent}/P_{tot} from 0.8 to 0.2 strongly mitigates the number and amplitude of large intermittent peaks in the data time series. This is consistent with a larger sheared flow that acts to break up turbulent structures moving into the far SOL.

A strong decrease in fluctuation amplitudes during ICRF heating was reported in other works as well [24–26], but here we show that this effect can be completely eliminated by mitigating the RF-induced E×B flows. We first calculate the normalized signal $(I - \langle I \rangle)/\langle I \rangle$ within the 280 ms time interval using a 5 ms moving time window to remove trends and low-frequency oscillations due, for example, to changes in the plasma position. In figure 7(*a*), we plot the conditionally-averaged waveform of $(I - \langle I \rangle)/\langle I \rangle$, obtained by calculating the average shape of features with peak amplitudes larger than 2.5 standard deviations. As P_{cent}/P_{tot} is decreased from 0.8 to 0.2, the amplitude of the average peak decreases significantly and, for $P_{cent}/P_{tot} = 0.8$, it is similar to that in the case without ICRF. To better understand what is shown in figure 7(*a*), it is perhaps useful to look back at figure 6, where the black dotted lines show the threshold of 2.5 standard deviations above which peaks are considered for the conditional averaging. Without ICRF, the conditional averaging only samples the high-amplitude intermittent peaks (corresponding to radially-propagating filaments). As P_{cent}/P_{tot} decreases from 0.8 to 0.2
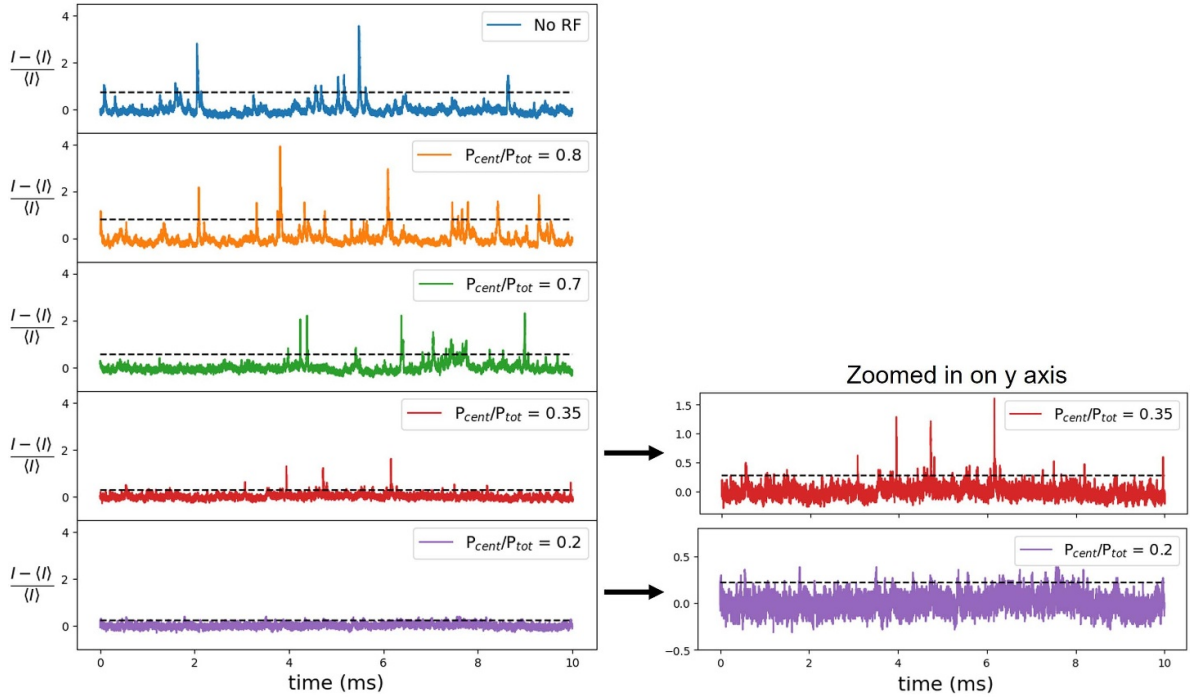
Figure 6. $(I - \langle I \rangle)/\langle I \rangle$ at $(\mathrm{R}, \mathrm{Z}) = (91.045, -1.974)$ cm over a 10 ms section of the 280 ms time window for the case without ICRF and the four cases with 1 MW of injected ICRF power and different power ratios. The black dotted line in each case corresponds $+2.5\ \delta I/\langle I \rangle$, which is the limit above which peaks are considered for the conditional averaging shown in figures 7(*a*) and 8(*a*). On the right, we zoom in on the *y* axis for the cases with the lowest two power ratios.

and high-amplitude fluctuations are suppressed, the standard deviation decreases and the conditional averaging samples the more numerous low-amplitude fluctuations that are closer to the center of the distribution.

References [24, 26] also showed the power spectrum and probability distribution function (PDF) of $(I_{sat} - \langle I_{sat} \rangle)$ (where I_{sat} was the ion saturation current signal measured by a fixed Langmuir probe in the far SOL). During ICRF heating, strong decreases in the low-frequency component of the power spectrum and of the large positive tail of the PDF were reported. This is also seen here in the power spectra and PDFs of $(I - \langle I \rangle)/\langle I \rangle$ (shown in figures 7(*b*) and (*c*) respectively), and these effects are amplified by decreasing the power ratio from 0.8 to 0.2. Moreover, the PDFs of the fluctuations are almost identical for the cases without RF and with 1 MW of ICRF but $P_{\mathrm{cent}}/P_{\mathrm{tot}} = 0.8$. Since these data samples have different standard deviations, the substantial decrease in the low-frequency oscillations in figure 7(*b*) and of the large positive tail of the distribution in figure 7(*c*) is indicative of the decrease in fluctuation amplitudes, as can be seen by comparing these figures with figure 7(*a*). This unambiguous dependence of fluctuation amplitudes on $P_{\mathrm{cent}}/P_{\mathrm{tot}}$ suggests that as the magnitude of the RF-induced E×B flow increases, less plasma is convected across the SOL by high-amplitude filaments. These results are consistent with the radially sheared poloidal E×B flow acting as a transport barrier that destroys radially moving density filaments, which would produce the effect observed in the fluctuation statistics.

For an analysis of turbulence properties that is independent of fluctuation amplitudes, we normalize the detected signal so

as to have a unit standard deviation, i.e. we study fluctuations of $\tilde{I} = (I - \langle I \rangle)/\delta I$ where $\langle I \rangle$ and δI are the mean and standard deviation of the detected signal. Again, this normalization is done using a moving 5 ms time window. Figure 8(*a*) shows the conditionally-averaged waveforms of $\tilde{I}$, normalized so that their maximum amplitude is equal to 1, which is necessary to compare the pulse duration times. As shown in figure 8(*a*), the duration time is generally smaller with ICRF than without ICRF, and it decreases when decreasing $P_{\mathrm{cent}}/P_{\mathrm{tot}}$ from 0.8 to 0.2, while the pulses in the cases with the two lowest power ratios (0.35 and 0.2) have more or less the same duration time. The full width at half maximum (FWHM) of each waveform is shown in the legend of figure 8(*a*) and can be used as a measure of pulse duration time. This decrease in pulse duration time can be interpreted in two ways. First, it is consistent with the blobs being accelerated by the poloidal E×B flow. Second, assuming Taylor's frozen turbulence hypothesis, it is also consistent with the reduction of large-scale turbulence structures and enhancement of small-scale structures. Given the strong decrease in fluctuation amplitudes observed in figure 7, which points to the suppression of large blobs, we argue that a combination of the two might be happening.

Figure 8(*b*) shows the power spectra $\mathrm{S}_f(\tilde{I})$ of the rescaled data. We can see that decreasing $P_{\mathrm{cent}}/P_{\mathrm{tot}}$ from 0.8 to 0.2 leads to a decrease in the low-frequency part of the spectra as well as an increase in the high-frequency part of the spectra. As with the conditionally-averaged waveforms, this could be consistent with the blobs being accelerated by the poloidal E×B flow and with large-scale structures being split into small-scale structures as the magnitude of the sheared E×B
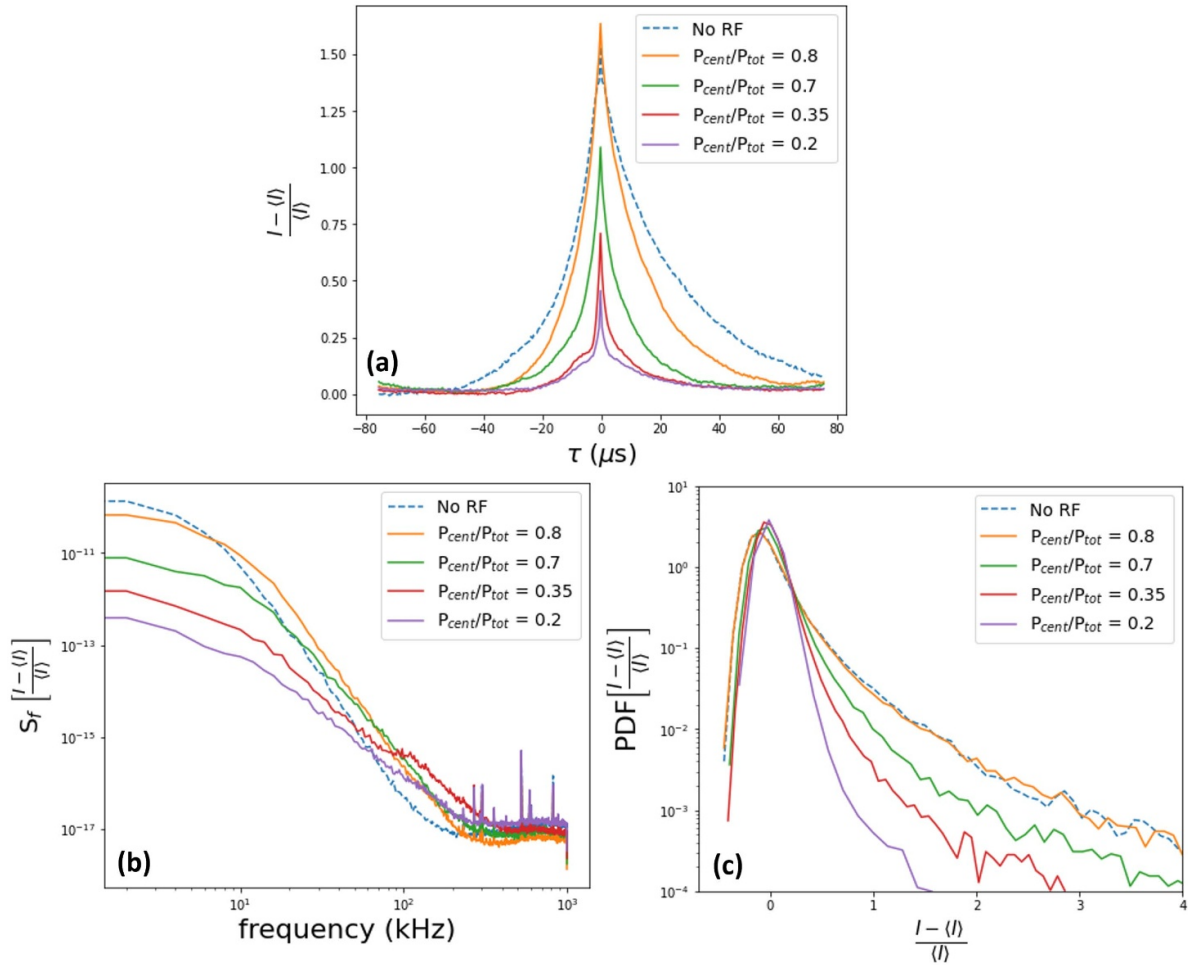
Figure 7. Statistical analysis of $(I - \langle I \rangle)/\langle I \rangle$ at $(R, Z) = (91.045, -1.974)$ cm for the case without ICRF and the four cases with 1 MW of injected ICRF power and different power ratios. (*a*) Conditionally-average waveforms obtained by calculating the average shape of features with peak amplitudes larger than 2.5 standard deviations. (*b*) Frequency power spectra S_f. The spikey features above 200 kHz are from the system electronics and the flat sections at high frequencies are indicative of the noise floor. (*c*) Probability distribution functions (PDF).

velocity increases. The noise floor also increases as $P_{\text{cent}}/P_{\text{tot}}$ is decreased from 0.8 to 0.2, which is a consequence of the decreasing standard deviation.

The PDF of the rescaled signal $\tilde{I}$ is shown in figure 8(*c*). We see that decreasing the power ratio from 0.8 to 0.2 leads to a decrease in the large positive tail of the distribution (corresponding to convective transport by large-amplitude filaments) as well as an increase in the negative part of the distribution. This is consistent with a stronger mitigation of SOL convective transport with increasing RF-induced E×B velocity and with the distribution function getting closer to a Gaussian (which would have a parabolic shape in a semi-logarithmic plot).

This is confirmed in figure 9, where we show the statistical moments of the fluctuations at $(R, Z) = (91.045, -1.974)$ cm. To properly determine these parameters and estimate their uncertainty, we use the method described in [38]: a random sample containing 75% of the data is selected and used to calculate the basic statistical properties. This process is then repeated 10 000 times. The data points in figure 9 correspond to the mean value of the estimated parameters while the error bars indicate two standard deviations about the mean. As shown in

figure 9(*a*), $\delta I / \langle I \rangle$ increases as $P_{\text{cent}}/P_{\text{tot}}$ is increased from 0.2 to 0.8. Most importantly, for $P_{\text{cent}}/P_{\text{tot}} = 0.8$, when the RF-induced E×B flow is the smallest, the normalized level of fluctuations becomes similar to that in the absence of ICRF. Similarly, the skewness and flatness also scale with $P_{\text{cent}}/P_{\text{tot}}$ (figures 9(*b*) and (*c*)), suggesting that the distribution function becomes closer to a Gaussian as $P_{\text{cent}}/P_{\text{tot}}$ is decreased from 0.8 to 0.2. However, note that the flatness is very sensitive to a few statistical outliers—single events with very large amplitudes that do not reflect the overall trend seen in the distribution function. While extremely rare and unrepresentative of the rest of the distribution function, these statistical outliers are enough to strongly increase the error bars in the flatness calculations. Excluding these outliers from our analysis hence allows us to better visualize the overall impact of power ratio modulation on the flatness of our distribution. As shown in figure 10(*a*), in the case with $P_{\text{cent}}/P_{\text{tot}} = 0.2$, only 2 events with amplitude larger than 17 standard deviations are detected (over a total of 1061 detected peaks with amplitude larger than 2.5 standard deviations). However, these are so far from the rest of the distribution that they can significantly increase
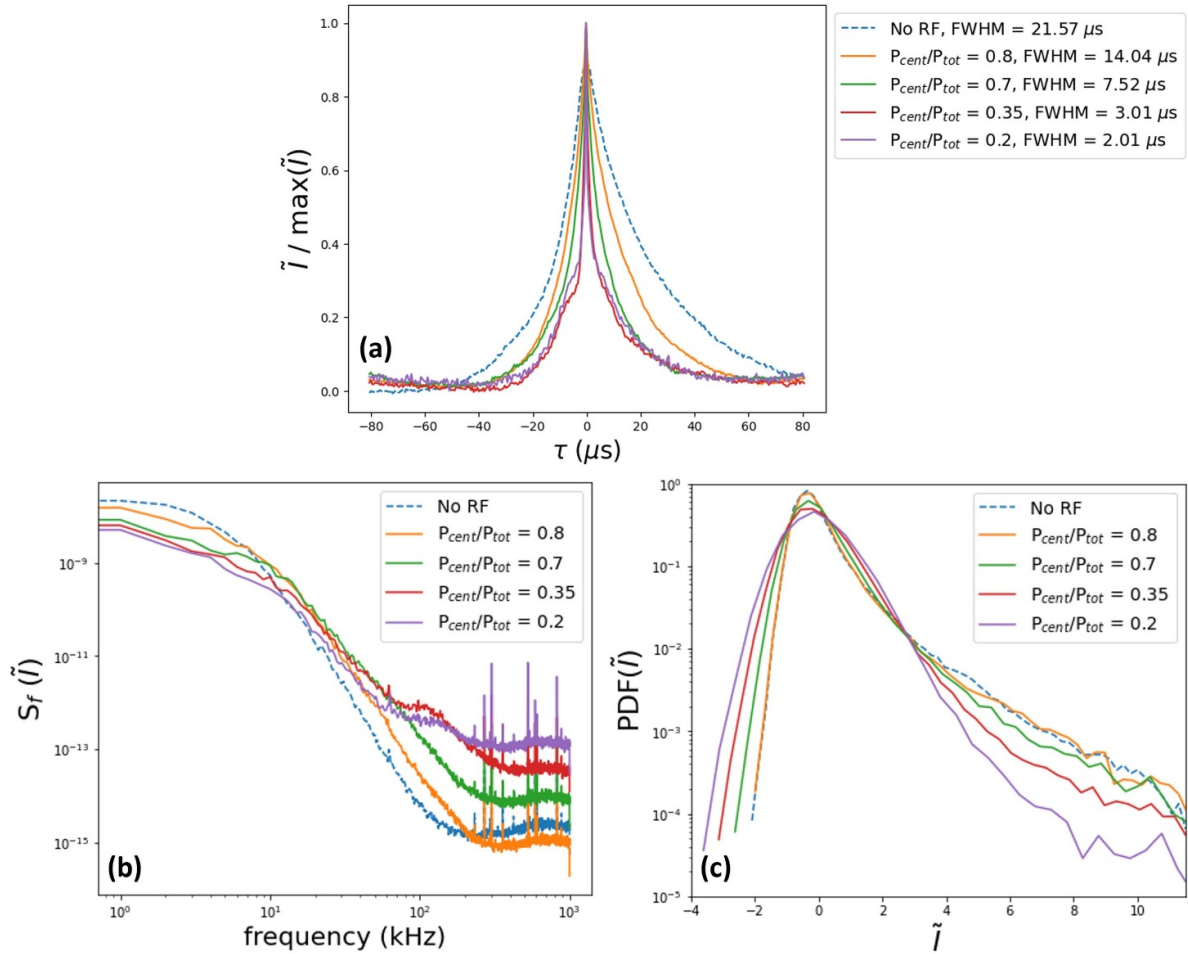
Figure 8. Statistical analysis of $\tilde{I} = (I - \langle I \rangle)/\delta I$ at (R,Z) = (91.045, −1.974) cm for the case without ICRF and the four cases with 1 MW of injected ICRF power and different power ratios. (*a*) Conditionally-averaged waveforms obtained by calculating the average shape of features with peak amplitudes larger than 2.5 standard deviations. The FWHM of each waveform is shown in the legend and used as a measure of pulse duration time. (*b*) Frequency power spectra S_f. The spikey features above 200 kHz are from the system electronics and the flat sections at high frequencies are indicative of the noise floor. (*c*) PDF of the time series.

the error bars in the flatness calculation. In figure 10(*b*), we show the flatness measured after eliminating statistical outliers with an amplitude larger than 17 standard deviations. A similar trend to that of the other statistical moments is seen (i.e. the flatness increases with power ratio and eventually becomes similar to its value measured without ICRF). This further indicates that the ICRF-induced E×B flow is responsible for reducing convective transport in the far SOL.

Moreover, these changes in the distribution function are localized in the far SOL, outside of the shear layer induced by ICRF. This can be seen in figure 11, where we show the statistical moments estimated at $R = 89.121$ cm, which is located inside the RF-induced shear layer (see figure 5). In this case, the standard deviation, skewness, flatness, and normalized fluctuation level are similar with and without ICRF and do not scale with power ratio. Similarly, the effect of ICRF on fluctuation amplitudes is also localized in the region outside the E×B shear layer. This is shown in figure 12, where we plot the conditionally-averaged waveforms of $(I - \langle I \rangle)/\langle I \rangle$ at $R = 89.121$ cm. In this case, the amplitude of the average peak is similar with and without ICRF and does not depend on

$P_{\text{cent}}/P_{\text{tot}}$. This is to be compared with the conditionally averaged waveforms at $R = 91.045$ cm shown in figure 7(*a*).

4. Direct observation of blob shearing by RF-induced flows

The aim of this section is to directly observe the interaction between blobs and RF-induced radially-sheared poloidal E×B flows and its consequences on convective transport in the SOL. To do so, we use data from the GPI-Phantom camera, which has a higher spatial resolution and is therefore appropriate for visualizing blob creation and propagation in the SOL. We compare two discharges (1150 709 031 and 1150 904 024) with similar plasma parameters (LSN, $B_T = 5.4$ T, $I_p = 1.1$ MA, $\bar{n}_e = 1.85 − 2.15 × 10^{20}$ m^{-3}), the first one relying solely on ohmic heating, and the second one being heated with 1 MW of ICRF from the two-strap D antenna. In these discharges, the GPI field of view was magnetically connected to the upper corner of the D antenna, similar to the case shown in figure 3.
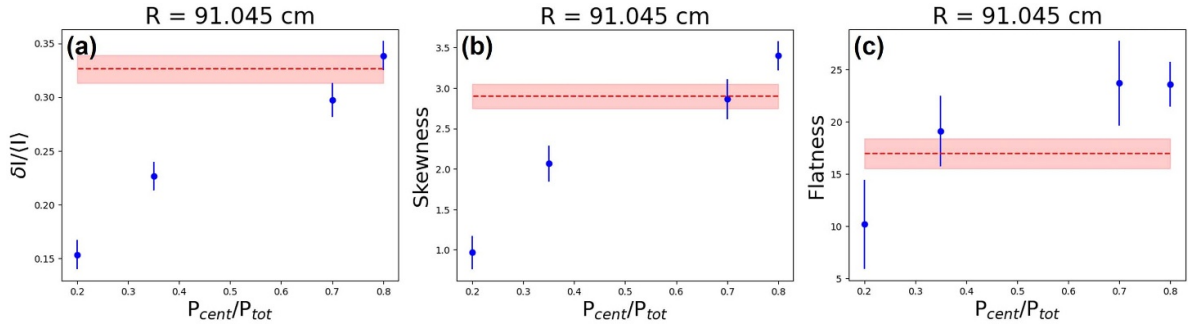
Figure 9. Relative fluctuation level $\delta I / \langle I \rangle$ (*a*), skewness (*b*), and flatness (*c*) of the detected signal at $(\text{R}, \text{Z}) = (91.045, -1.974)$ cm (farther into the SOL than the shear layer, see figure 5) as a function of $P_{\text{cent}}/P_{\text{tot}}$. The red dashed lines and red shaded areas correspond to the estimated values and error bars for the case without RF.

(a)

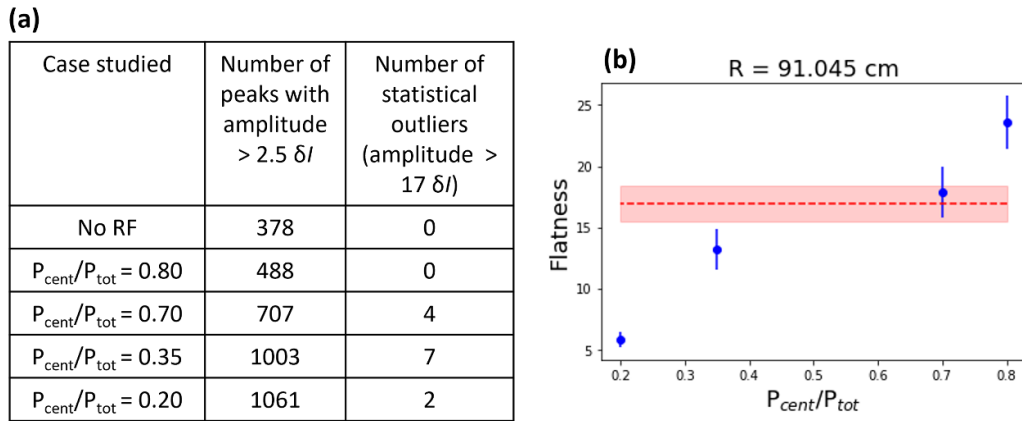| Case studied	Number of peaks with amplitude > 2.5 δI	Number of statistical outliers (amplitude > 17 δI)
No RF	378	0
$P_{\text{cent}}/P_{\text{tot}} = 0.80$	488	0
$P_{\text{cent}}/P_{\text{tot}} = 0.70$	707	4
$P_{\text{cent}}/P_{\text{tot}} = 0.35$	1003	7
$P_{\text{cent}}/P_{\text{tot}} = 0.20$	1061	2

Figure 10. (*a*) Table showing the number of peaks with amplitude larger than 2.5 δI and the number of statistical outliers (amplitude larger than 17 δI) for the 5 cases studied. (*b*) Flatness calculation after removing the outliers from the data, to be compared with the 'uncorrected' flatness calculation shown in figure 12.
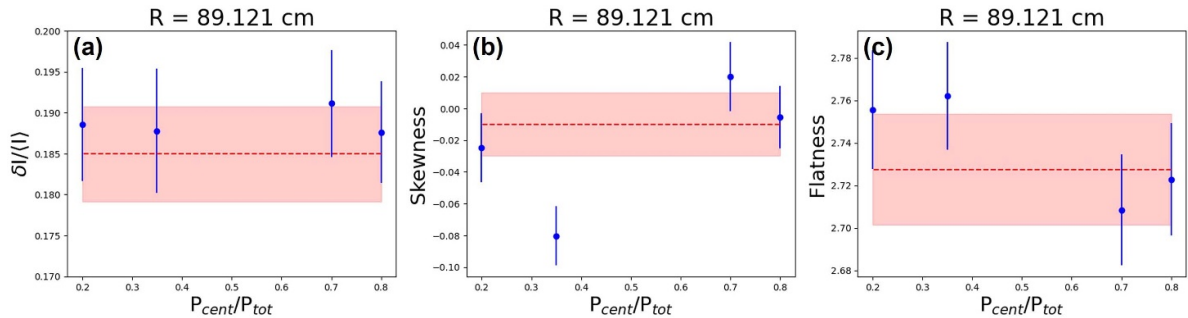

Figure 11. Relative fluctuation level $\delta I / \langle I \rangle$ (*a*), skewness (*b*), and flatness (*c*) of the detected signal at $(\text{R}, \text{Z}) = (89.121, -1.582)$ cm (closer to the plasma than the shear layer, see figure 5) as a function of $P_{\text{cent}}/P_{\text{tot}}$. The red dashed lines and red shaded areas correspond to the estimated values and error bars for the case without RF.

Given that this experiment was performed with a two-strap antenna, modulation of $P_{\text{cent}}/P_{\text{tot}}$ was not possible in this case, and we did not have control over the magnitude of RF-induced E×B flows. However, previous experiments have shown that with dipole phasing (180° phase difference between neighboring straps) the two-strap D antenna produces similar RF-enhanced potentials as the four-strap field-aligned J antenna with $P_{\text{cent}}/P_{\text{tot}} = 0.5$ [16]. Accordingly, since the experiment presented in this section and those discussed in section 3 were done with the same total amount of injected ICRF power

(1 MW), we expect the image currents on the structure of the D antenna and the resulting E×B flows to be similar to those produced by the four-strap J antenna (section 3) with $P_{\text{cent}}/P_{\text{tot}} = 0.5$.

First, to visualize the impact of ICRF heating on SOL flow, we apply a cross-correlation technique to the 64×64 array of views available using the GPI-Phantom system in order to calculate a 2D map of the vertical velocity v_Z in the GPI-Phantom field of view. The result is shown in figure 13, where we focus on the region of interest that contains the ICRF-induced $E \times B$
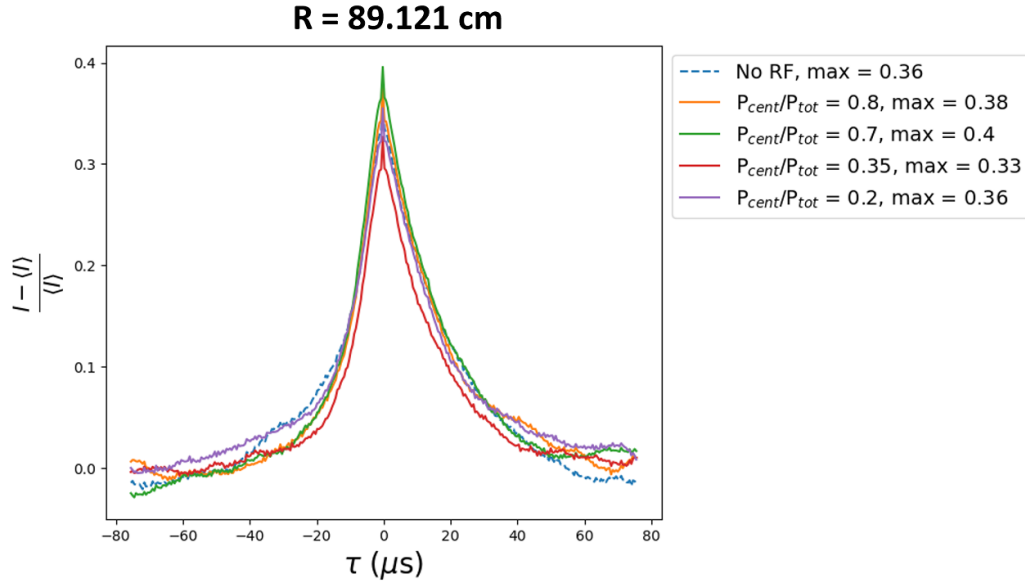
Figure 12. Conditionally-averaged waveforms of $(I - \langle I \rangle)/\langle I \rangle$ at $(R, Z) = (89.121, -1.582)$ cm for the case without ICRF and the four cases with 1 MW of injected ICRF power and different power ratios. The waveforms are obtained by calculating the average shape of all features with peak amplitudes larger than 2.5 standard deviations. The maximum value of each waveform is shown in the legend.
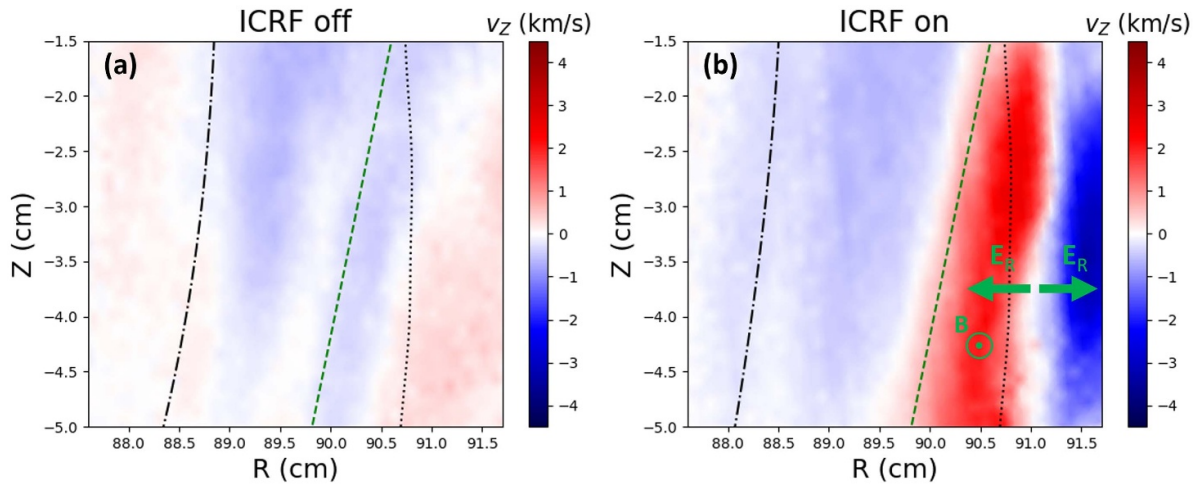

Figure 13. 2D map of the vertical velocity in a portion of the GPI-Phantom field of view (*a*) without ICRF and (*b*) with ICRF. The black dash-dotted line shows the LCFS position estimated using EFIT. The green dashed line shows the approximate location of the innermost shear layer. It will also be used as a 'finish line' to count the number of blobs that make it into the far SOL. The black dotted line shows the position of the ICRF antenna limiter, magnetically mapped to the GPI field of view.

flows. In the absence of ICRF, the vertical velocity in the SOL is in the range $[-1.5, 0.5]$ km s^{-1}. During ICRF heating, two regions can be distinguished: one where the flow is similar to that without ICRF, and one with much larger vertical velocities, of magnitude closer to 2 km s^{-1}. Consequently, the vertical velocity is strongly sheared between these two regions. The green dashed line in figure 13 marks the approximate location of this innermost shear layer and roughly separates these two regions. Also note the complexity of the flow pattern in the region to the right of the green dashed line: the flow changes direction around $R = 91$ cm and, at $R = 91.5$ cm, it has large negative values, up to -4.5 km s^{-1}. With the background magnetic field pointing out of the page, this indicates that RF-induced DC radial electric fields $\mathbf{E}_R$ point in opposite

directions at $R \approx 91$ cm, as represented by the green arrows in figure 13.

To study the interaction of these $E \times B$ flows with SOL filaments, we apply a newly developed machine learning-based blob tracking algorithm [28] to the GPI data from the two discharges over a time window of 47 ms. Of the four baseline methods implemented, we choose to use the RAFT model, as it was shown to perform best in [28]. In total, the algorithm detects 780 blobs in the case without ICRF and 942 blobs in the case with ICRF. In figures 14(*a*) and (*b*), we plot the trajectories of 300 randomly selected blobs for the cases without and with ICRF respectively. Significant differences can be seen in the blob trajectories between the two cases. Without ICRF, all blobs are generated in the field of view close to the LCFS and
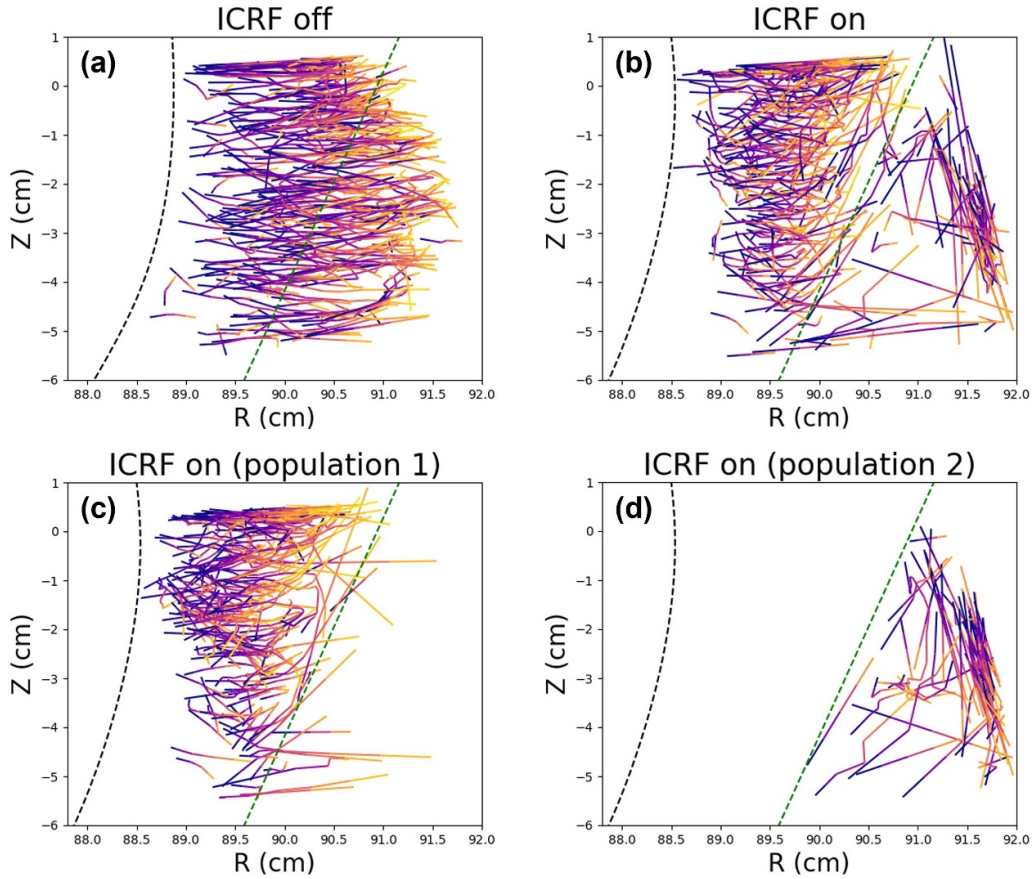
Figure 14. (*a*) Trajectories of 300 randomly selected blobs in the case without ICRF. (*b*) Trajectories of 300 randomly selected blobs in the case with ICRF. (*c*) Trajectories of 225 randomly selected blobs from population 1 (ICRF on). (*d*) Trajectories of 75 randomly selected blobs from population 2 (ICRF on). The colors go from blue to yellow along the trajectory of each blob.

propagate radially toward the wall. With ICRF, two different populations of blobs can be seen: blobs that are created in the field of view near the LCFS and propagate radially outward (population 1) and blobs that are convected by the E×B flow from above or below the field of view (population 2). These two populations of blobs can be roughly separated by whether they are first detected to the right or to the left of the shear layer (green dashed line in figures 13 and 14). In the case with ICRF, roughly 75% of detected blobs belong to population 1. In figure 14(*c*), we plot the trajectories of 225 randomly selected blobs belonging to population 1, and in figure 14(*d*), we plot the trajectories of 75 randomly selected blobs belonging to population 2. Two important observations can be made from these trajectories. First, notice that most blobs from population 1 are destroyed before crossing the green dashed line (which we refer to as the 'finish line'). On the other hand, without ICRF, most blobs are seen to propagate radially beyond the finish line. Using the blob-tracking algorithm, we can calculate the proportion of blobs that cross the finish line in the two cases. Without ICRF, we find that roughly 57% of detected blobs cross the finish line, while only 8% of detected blobs cross the line in the case with ICRF. This is an indication that the RF-induced radially-sheared E×B flow acts as a transport barrier that prevents large blobs from propagating far into the SOL. Moreover, as shown in figure 14(*d*), most

of the fluctuations detected to the right of the finish line (population 2) have nearly vertical trajectories. We speculate that these correspond to blobs that have made it through the shear layer either above or below the field of view and that have been convected vertically by the E×B flow.

Another way to visualize these results is to look at a histogram of the first and last major radii of the tracked blobs. As shown in figure 15, without ICRF, a single peak appears in the distribution functions, corresponding to blobs moving radially through the SOL into the far SOL. With ICRF, two different peaks can be seen in the distributions. The peaks on the left in figures 15(*a*) and (*b*) correspond to the blobs of population 1, which are born in the near SOL but move only a short distance ($\sim$10 mm) radially outward. As shown in figure 15(*b*), these blobs do not make it as far radially as those detected without ICRF. The second peaks at the right of the distributions shown in figures 15(*a*) and (*b*) correspond to the blobs of population 2, which are convected upward or downward by the flow. Contrary to the blobs from population 1, these blobs propagate mostly vertically, which explains why this peak has almost the same position in the two histograms.

In figure 16, the histograms of the average radial velocity $\langle v_R \rangle$ estimated using the blob tracking algorithm are shown for the different cases studied. For both populations of blobs detected during ICRF heating, $\langle v_R \rangle$ is on average smaller.
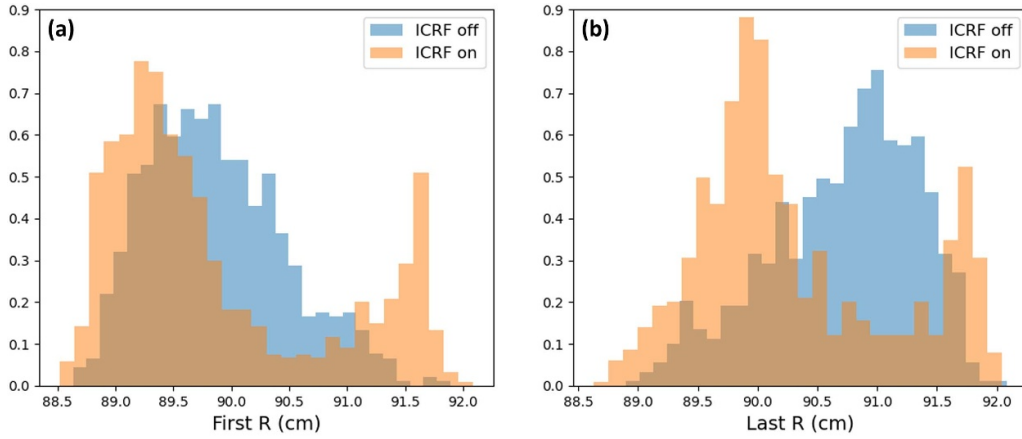
Figure 15. (*a*) Histograms of the first major radius of detection of the blobs. (*b*) Histograms of the last major radius of detection of the blobs.
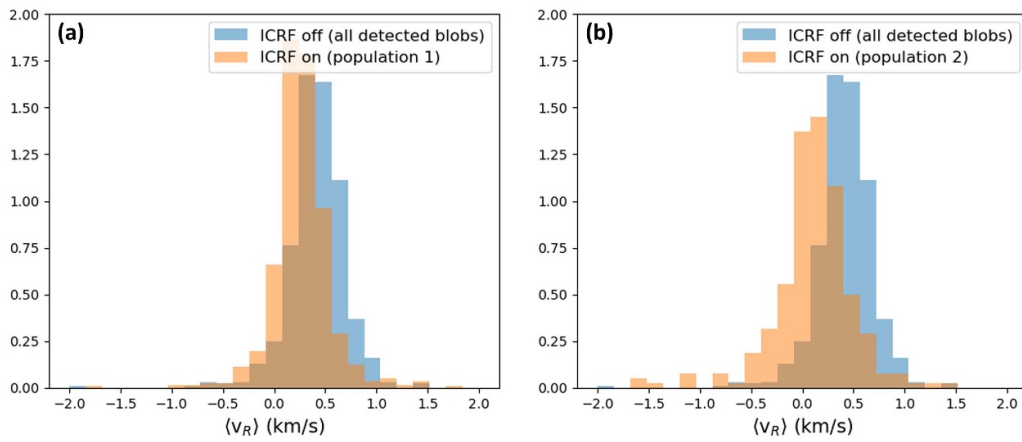

Figure 16. Histograms of the average radial velocity $\langle v_R \rangle$ of detected blobs for the cases with and without ICRF. For the case with ICRF, (*a*) considers only population 1 while (*b*) considers only population 2.

The fact that the radial velocity is smaller for the blobs of population 1 (mean value of $0.27\,\mathrm{km\,s^{-1}}$ vs. $0.41\,\mathrm{km\,s^{-1}}$ without ICRF) is likely due to the slowing down and destruction of the blobs as they reach the shear layer. For the blobs of population 2, $\langle v_R \rangle$ is substantially lower (mean value of $0.10\,\mathrm{km\,s^{-1}}$ vs. $0.41\,\mathrm{km\,s^{-1}}$ without ICRF) and even has a small negative tail. This is because these blobs mostly follow the E×B flow and do not exhibit the usual outward radial motion.

In figure 17, the histograms of the average vertical velocity $\langle v_Z \rangle$ estimated using the blob tracking algorithm are plotted for the different cases studied. As expected, blobs from population 1, which propagate mostly radially before getting destroyed by the shear layer, have a similar vertical velocity distribution to those without ICRF. On the other hand, the $\langle v_Z \rangle$ distribution for blobs of population 2 is skewed to large positive and negative values, which is consistent with the cross-correlation analysis shown in figure 13. Note, however, that the two methods are not measuring exactly the same thing: the cross-correlation analysis provides information about the velocity field at each point in the field of view while the blob-tracking algorithm provides information about the velocity of large blobs as they move along their trajectories in the field of view.

Moreover, note that blobs that make it inside the E×B cell have very different shapes from those that do not. This can be seen in figure 18, where we plot the distribution of the average elongation of the blobs detected in the different cases. This is estimated using the following formula

$$\text{elongation} = \frac{\delta R \cdot \delta Z}{\text{blob area}} \cdot \frac{\max(\delta R, \delta Z)}{\min(\delta R, \delta Z)}, \qquad (1)$$

where δR and δZ are the radial and vertical extents of the tracked blobs respectively. We can convince ourselves that this is a good measure of a blob's elongation except for star-shaped blobs, which are never observed. As shown in figure 18, blobs from population 1 have similar average elongations to those without ICRF (the distribution is slightly skewed to larger average elongations, which is likely due to the stretching of blobs by the sheared flow close to the finish line where they are being destroyed). However, blobs from population 2 have a much more distinct elongation distribution, with a large positive tail and a higher average value (3.18 vs. 1.8 without ICRF).

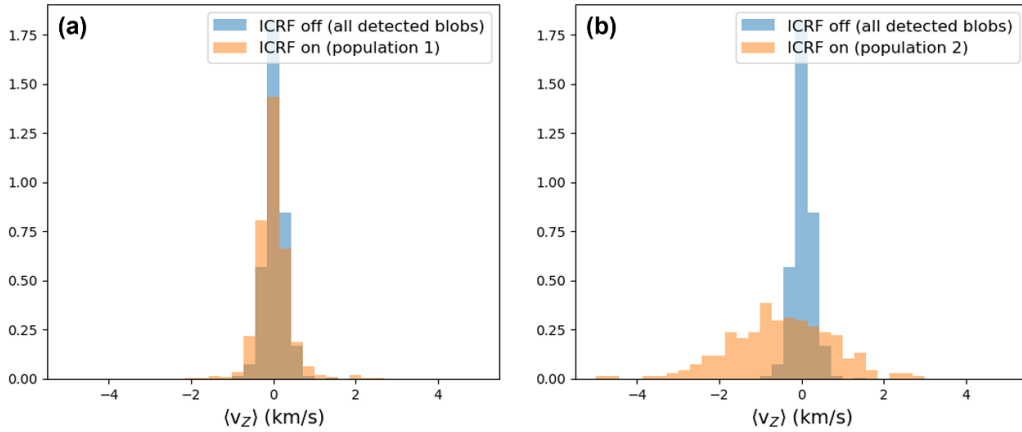From the analysis presented above, the following can be concluded:

Figure 17. Histograms of the average vertical velocity $\langle v_Z \rangle$ for the cases with and without ICRF. For the case with ICRF, (*a*) considers only population 1 while (*b*) considers only population 2.
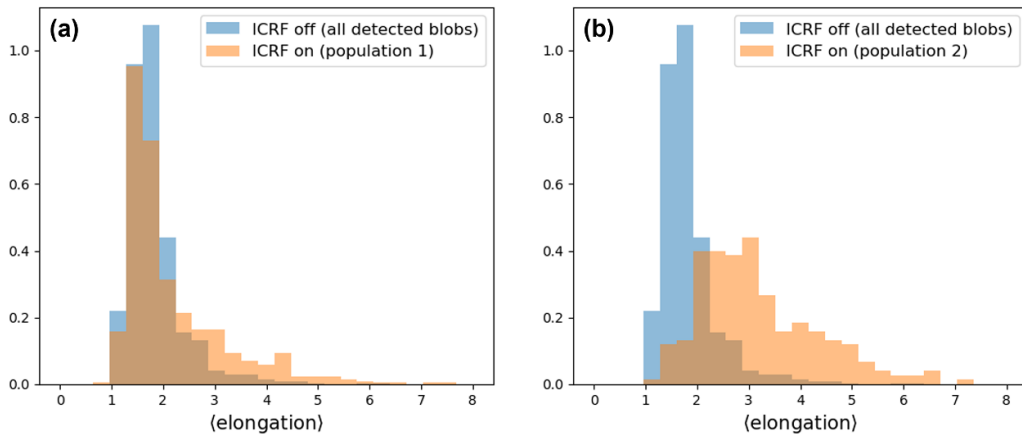

Figure 18. Histograms of the average blob elongation for the cases with and without ICRF. For the case with ICRF, (*a*) considers only population 1 while (*b*) considers only population 2.

- In the absence of ICRF, tracked blobs are born in the near SOL and propagate through the SOL into the far SOL. They have low elongation (average value of 1.8) and average radial velocities of $0.41\,\mathrm{km\,s^{-1}}$.
- During ICRF heating, the radially-sheared E×B flow acts as a transport barrier that slows down, stretches, and destroys most of the radially-moving blobs. As such, we find that only 8% of the detected blobs cross the finish line in the case with ICRF, as opposed to 57% without ICRF.
- The few blobs that make it inside the large-flow region are therefore highly elongated (average value of 3.18). They appear as being convected by the flow from above or below the field of view. Their average radial velocity is significantly smaller ($\approx 0.1\,\mathrm{km\,s^{-1}}$) and their vertical velocity is large (both positive or negative, of the order of a few $\mathrm{km\,s^{-1}}$).

Overall, taking into account both populations of blobs, we find that fewer blobs are detected to the right of the finish line during ICRF heating (296 blobs with ICRF vs. 514 without ICRF). Moreover, blobs that have reached this region (after being slowed down radially and stretched) are less distinguishable from the background flow than those detected without

ICRF. This can be seen by calculating the ratio of the mean amplitude of detected blobs to the mean value of the GPI signal in the region to the right of the finish line. We find that this ratio is equal to 4.60 in the case without ICRF but only 1.67 in the case with ICRF. As a consequence of this complex interaction, the relative fluctuation level $\delta I / \langle I \rangle$ in the far SOL decreases significantly, as shown in figure 19. This is consistent with the observations made in section 3 using data from the GPI-APD diagnostic.

5. Conclusion and discussion

In this work, the interaction between ICRF-induced radially-sheared poloidal E×B flows and turbulent filaments in the SOL was investigated. As reported in previous studies [23–27], we have found that ICRF heating strongly mitigates intermittent fluctuations in the far SOL (in regions magnetically connected close to the antenna), hence leading to a reduction in convective radial transport. The relationship between this observation and RF-induced E×B flows was elucidated. This was done by controlling the amplitude of these flows by varying antenna power ratio $P_{\mathrm{cent}}/P_{\mathrm{tot}}$ and by studying the resulting
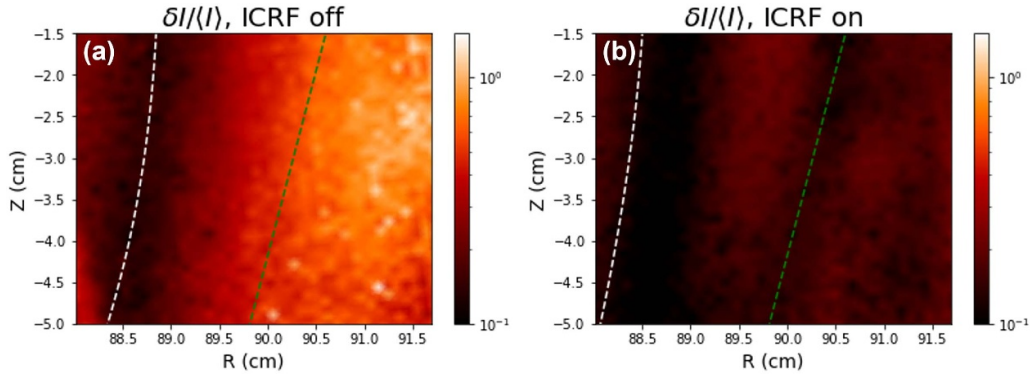
Figure 19. Relative fluctuation level in the GPI field of view for the cases (*a*) without ICRF and (*b*) with ICRF. The color bar is in the log scale.

changes in turbulence properties. We have found that decreasing P_{cent}/P_{tot} from 0.8 to 0.2 (which increases the magnitudes of the E×B flows) enhances the turbulence-canceling effect of ICRF. On the other hand, this effect could be reversed or even eliminated by increasing the power ratio so as to mitigate the magnitude of the flows. As such, we argue that RF-induced E×B flows play a dominant role in the somewhat universal reduction in SOL convective radial transport during ICRF heating.

We then applied a machine learning-based blob tracking algorithm [28] to high-resolution GPI videos in order to directly observe the impact of RF-induced radially-sheared poloidal flows on blob propagation in the SOL. We have shown that these radially sheared flows can slow down, stretch, and destroy the radially moving blobs. A finish line was defined to coincide roughly with the location of the innermost shear layer. A factor of 7 reduction in the proportion of tracked blobs that cross the finish line was found during ICRF heating. Those blobs that make it through the shear layer are highly elongated and have low radial velocities and high vertical velocities, essentially following the background E×B flow. A consequence of this complex interaction is a net decrease in the relative fluctuation level in the region outside the innermost shear layer.

This interaction likely plays an important role in the commonly observed modifications of the edge density distribution during ICRF heating. The accumulation and destruction of filaments near the shear layer will likely increase the density in this region and reduce the density in the center of the convective cell, which is inaccessible to most filaments. Moreover, the flow will likely carry around its over-density and redistribute the density in the SOL, which can render SOL density profiles poloidally asymmetric [19]. This picture is consistent with the complex density patterns measured in multiple experiments, which have been discussed in the introduction. In this work, we have also shown that an optimal P_{cent}/P_{tot} can strongly mitigate this interaction by reducing the magnitude of RF-induced flows. While edge density profile measurements in regions magnetically connected to the antenna were not available during these experiments, we expect the impact of ICRF on edge density (and on lower hybrid wave coupling) to also depend on power ratio.

Finally, we would expect the process of blob shearing by ICRF-induced E×B flows to mitigate peak heat and particle fluxes to the first wall and divertor regions due to turbulent filaments or ELMs in places that are magnetically connected sufficiently close to the antenna. However, the ICRF-enhanced plasma potentials driving these E×B flows are also expected to accelerate ions toward the antenna limiters causing enhanced heat fluxes, sputtering, and material degradation. Consequently, we do not believe that ICRF would be an efficient tool for mitigating heat fluxes in future reactors. From the perspective of the ICRF operator, it is usually sought to reduce impurity contamination, antenna heat fluxes, and unwanted wave-SOL interaction, thus minimizing RF-induced radial electric fields. As shown in this study, this would also reduce the turbulence-cancelling properties of ICRF.

ORCID iDs

R. Diab ⬤ https://orcid.org/0000-0003-4206-5868
G. Decristoforo ⬤ https://orcid.org/0000-0002-7616-0946
S. Ahmed ⬤ https://orcid.org/0000-0002-7732-5765
J.L. Terry ⬤ https://orcid.org/0000-0003-4255-5509

References

[1] Lin Y., Wright J.C. and Wukitch S.J. 2020 Physics basis for the ICRF system of the SPARC tokamak *J. Plasma Phys.* **86** 865860506

[2] Lamalle P.U. *et al* 2009 Status of the ITER IC H&CD system *AIP Conf. Proc.* **1187** 265

[3] Noterdaeme J.M. and Van Oost G. 1993 The interaction between waves in the ion cyclotron range of frequencies and the plasma boundary *Plasma Phys. Control. Fusion* **35** 1481

[4] Bures M., Brinkschulte H., Jacquinot J., Lawson K.D., Kaye A. and Tagle J.A. 1988 The modification of the plasma edge and impurity production by antenna phasing during ICRF heating on JET *Plasma Phys. Control. Fusion* **30** 149

[5] Tanaka T., Majeski R., Diebold D.A. and Hershkowitz N. 1996 RF generated voltage on the Faraday screen of an ICRF antenna and its effect on the Phaedrus-T edge plasma *Nucl. Fusion* **36** 1609

[6] Messiaen A. *et al* 1989 Effect of antenna phasing and wall conditioning on ICRH in TEXTOR *Plasma Phys. Control. Fusion* **31** 921

[7] Hanson G.R., Bush C.E., Wilgen J.B., Bigelow T.S., Rogers J.H. and Wilson J.R. 2008 Measurements of edge density profile modifications during IBW on TFTR *AIP Conf. Proc.* **403** 451

[8] Colas L. *et al* 2007 Understanding the spatial structure of RF-induced SOL modifications *Plasma Phys. Control. Fusion* **49** B35

[9] Colas L. *et al* 2007 2-D mapping of ICRF-induced SOL perturbations in Tore Supra tokamak *J. Nucl. Mater.* **363–365** 555–9

[10] Colas L. *et al* 2018 2D mappings of ICRF-induced SOL density modifications on JET *45th EPS Conf. on Plasma Physics (Prague, Czech Republic)* vol 42A

[11] Lau C., Lin Y., Wallace G., Wukitch S.J., Hanson G.R., Labombard B., Ochoukov R., Shiraiwa S. and Terry J. 2013 Effects of ICRF power on SOL density profiles and LH coupling during simultaneous LH and ICRF operation on Alcator C-Mod *Plasma Phys. Control. Fusion* **55** 095003

[12] Martin M.J., Gekelman W., Van Compernolle B., Pribyl P. and Carter T. 2017 Experimental observation of convective cell formation due to a fast wave antenna in the large plasma device *Phys. Rev. Lett.* **119** 205002

[13] Lau C. 2013 Effects of RF power on SOL density profiles and RF coupling on the Alcator C-Mod tokamak *PhD Thesis* Massachusetts Institute of Technology

[14] Ekedahl A. *et al* 2007 RF coupling and antenna heat load control for combined LHCD and ICRH in Tore Supra *AIP Conf. Proc.* **933** 237

[15] Cziegler I., Terry J.L., Wukitch S.J., Garrett M.L., Lau C. and Lin Y. 2012 Ion-cyclotron range of frequencies in the scrape-off-layer: fine structure radial electric fields *Plasma Phys. Control. Fusion* **54** 105019

[16] Wukitch S.J. *et al* 2013 Characterization and performance of a field aligned ion cyclotron range of frequency antenna in Alcator C-Mod *Phys. Plasmas* **20** 056117

[17] Hong R., Wukitch S.J., Lin Y., Terry J.L., Cziegler I., Reinke M.L. and Tynan G.R. 2017 Characterization of SOL plasma flows and potentials in ICRF-heated plasmas in Alcator C-mod *Plasma Phys. Control. Fusion* **59** 105008

[18] Colas L. *et al* 2021 The geometry of the ICRF-induced wave–SOL interaction. A multi-machine experimental review in view of the ITER operation *Nucl. Fusion* **62** 016014

[19] Bécoulet M., Colas L., Pécoul S., Gunn J., Ghendrih P., Bécoulet A. and Heuraux S. 2002 Edge plasma density convection during ion cyclotron resonance heating on Tore Supra *Phys. Plasmas* **9** 2619

[20] Garcia O.E., Fritzner S.M., Kube R., Cziegler I., Labombard B. and Terry J.L. 2013 Intermittent fluctuations in the Alcator C-Mod scrape-off layer *Phys. Plasmas* **20** 055901

[21] Antar G.Y., Counsell G., Yu Y., Labombard B. and Devynck P. 2003 Universality of intermittent convective transport in the scrape-off layer of magnetically confined devices *Phys. Plasmas* **10** 419

[22] Grulke O., Terry J.L., Cziegler I., Labombard B. and Garcia O.E. 2014 Experimental investigation of the parallel structure of fluctuations in the scrape-off layer of Alcator C-Mod *Nucl. Fusion* **54** 043012

[23] Morisaki T., Komori A., Nishimura K., Morita S., Motojima O., Iguchi H., Kawai Y., Matsuoka K., Okamura S. and Yamada H. 1995 Edge plasma behaviour during auxiliary heating in the compact helical system (CHS) *Plasma Phys. Control. Fusion* **37** 787

[24] Antar G., Assas S., Bobkov V., Noterdaeme J.-M., Wolfrum E., Herrmann A. and Rohde V. 2010 Convective transport suppression in the scrape-off layer using ion cyclotron resonance heating on the ASDEX Upgrade tokamak *Phys. Rev. Lett.* **105** 165001

[25] Antar G.Y., Goniche M., Ekedahl A. and Colas L. 2012 The role of power and magnetic connection to the active antenna in the suppression of intermittent structures by ion cyclotron resonance heating *Nucl. Fusion* **52** 103005

[26] Li Y.C. *et al* 2022 Experimental investigation on effect of ion cyclotron resonance heating on density fluctuation in SOL at EAST *Nucl. Eng. Technol.* **54** 207–19

[27] Antar G., Goniche M., Ekedahl A. and Colas L. 2014 On the interaction between the ion cyclotron resonance heating and scrape-off layer turbulence via coherent waves *Nucl. Fusion* **54** 083018

[28] Han W., Pietersen R.A., Villamor-Lora R., Beveridge M., Offeddu N., Golfinopoulos T., Theiler C., Terry J.L., Marmar E.S. and Drori I. 2022 Tracking blobs in the turbulent edge plasma of a tokamak fusion device *Sci. Rep.* **12** 18142

[29] Hutchinson I.H. *et al* 1998 First results from Alcator-C-MOD* *Phys. Plasmas* **1** 1511

[30] Cziegler I. 2011 Turbulence and transport phenomena in edge and scrape-off-layer plasmas *PhD Thesis* Massachusetts Institute of Technology

[31] Zweben S.J., Terry J.L., Stotler D.P. and Maqueda R.J. 2017 Invited review article: gas puff imaging diagnostics of edge plasma turbulence in magnetic fusion devices *Rev. Sci. Instrum.* **88** 041101

[32] Baek S.G., Terry J., Psfc M., Stotler D.S., Brunner D., Labombard B.L. and Baek S.G. 2016 Comparisons of measured gas puff emissions with DEGAS 2 modeling of Alcator C-Mod plasmas *Bulletin of the American Physical Society* vol 61

[33] Bobkov V. *et al* 2019 Impact of ICRF on the scrape-off layer and on plasma wall interactions: from present experiments to fusion reactor *Nucl. Mater. Energy* **18** 131–40

[34] Bobkov V. *et al* 2016 Making ICRF power compatible with a high-Z wall in ASDEX Upgrade *Plasma Phys. Control. Fusion* **59** 014022

[35] Ochoukov R., Whyte D.G., Brunner D., D'Ippolito D.A., Labombard B., Lipschultz B., Myra J.R., Terry J.L. and Wukitch S.J. 2013 ICRF-enhanced plasma potentials in the SOL of Alcator C-Mod *Plasma Phys. Control. Fusion* **56** 015004

[36] Urbanczyk G., Fedorczak N., Gunn J., Colas L., Li J.G. and Wang K. 2021 Perspective of analogy between heat loads and impurity production in L-mode discharges with ICRH in WEST *Nucl. Mater. Energy* **26** 100925

[37] Colas L., Bobkov V., Carralero D., Kočan M., Müller H.W., Manz P., Kubič M., Gunn J.P., Herrmann A. and Rohde V. (ASDEX-Upgrade team) 2015 2-dimensional mapping of ICRF-induced scrape-off layer modifications with a retarding field analyser on ASDEX-Upgrade *AIP Conf. Proc.* **1580** 259

[38] Kuang A.Q., LaBombard B., Brunner D., Garcia O.E., Kube R. and Theodorsen A. 2019 Plasma fluctuations in the scrape-off layer and at the divertor target in Alcator C-Mod and their relationship to divertor collisionality and density shoulder formation *Nucl. Mater. Energy* **19** 295–9